RSC Advances

PAPER

View Article Online
View Journal | View Issue

Cite this: *RSC Adv.*, 2020, **10**, 28965

The construction of the novel magnetic prodrug Fe_3O_4@DOX and its antagonistic effects on hepatocarcinoma with low toxicity

Jun Li,†[ab] Liang Li,†[c] Yang Lv,†[ab] Hao Zou,[d] Yanping Wei,[c] Fei Nie,[b] Wanli Duan,[b] Maidinamu Sedike,[a] Liang Xiao*[b] and Mei Wang *[a]

Received 23rd February 2020
Accepted 6th July 2020

DOI: 10.1039/d0ra01729a

rsc.li/rsc-advances

Doxorubicin (DOX) is widely used as a chemotherapeutic agent for liver cancer. However, its clinical applications are greatly restricted by its nonselective cytotoxicity. A novel magnetic prodrug, Fe_3O_4@DOX, was designed, synthesized and characterized, and Fe_3O_4 and DOX were connected by the peptide CGGAAN. The magnetic prodrug Fe_3O_4@DOX was successfully synthesized with average sizes of 95 nm and 322.5 nm by TEM (transmission electron microscopy) and Malvern Zetasizer instrument respectively. The maximum emission wavelength shifted from 594 nm for free DOX to 615 nm for conjugated DOX in the synthesized Fe_3O_4@DOX. Both free DOX and Fe_3O_4@DOX show strong cytotoxicity to legumain overexpressing PLC through apoptosis. Similarly, Fe_3O_4@DOX and DOX equally reduced tumor volume and induced cell apoptosis in tumor tissues, while the former significantly maintained body weight and extended the life of nude mice, therefore serving as a promising nanocarrier for liver cancer treatment.

1. Introduction

According to GLOBOCAN data, liver cancer is largely a problem in the less developed regions with an estimated 841 000 new cases and 782 000 deaths annually.[1–4] Its mortality ranks second in tumor-related deaths worldwide. In China, there were 466 100 new cases and 422 100 deaths from liver cancer in 2015, both occupying more than half of those all over the world.[5,6] Since the majority of patients with liver cancer are already in an advanced stage, the rate of surgical resection, which is the most thorough treatment, is only 20–30%.[7] Alternatively, hepatic artery intervention is commonly used and particularly preferred in patients who cannot undergo surgery. However, liver cancer is prone to both intrahepatic and extrahepatic metastasis, making it difficult to control distant metastasis through local treatments. Therefore, it is extremely important to improve the targeting of drugs to tumor cells as well as to decrease the toxicity of the targeted drugs.

The primary task of the drug delivery system is to specifically exert the anti-cancer effects in a therapeutic dose without large toxic effects or side effects. Recent advances have confirmed the value of nanocomposite drugs or nanomaterials for tumor targeted diagnosis and therapy.[8–11] For example, the porous nanogold embedded cellulose grafted polyacrylamide (PAM/C/Au) nanocomposite hydrogel were assembled, which enhanced the thermal and rheological properties make it an ideal carrier for ciprofloxacin.[12] Meanwhile, the technologies including focused magnetic field, laser, and radio frequency and microwave are also widely implemented in the drug delivery systems, among which the magnetic nanoparticles (MNPs) are of particular interest due to its harmless and can be specifically manipulated and localized in the tumor issue by remote magnetic fields.[13–16] Compared to other kinds of nanoparticles, the advantages of MNPs such as pure metals (Fe, Co, Ni, *etc.*), alloys (FeCo, alnico, permalloy, *etc.*), and oxides (γ-Fe_2O_3, $CoFe_2O_4$, Fe_3O_4, *etc.*) include small volume, large specific surface area, chemical modification on the surface, and good biocompatibility.[17–20] Moreover, the MNPs *e.g.* Fe_3O_4 can actively accumulate in tumor tissues through a pathway known as the enhanced permeability and retention (EPR) effect due to the hyperpermeable and dynamic opening of vasculature (vascular bursts) and the poor lymphatic drainage from tumor tissues.[21,22]

Legumain (LGMN), also referred to as asparaginyl endopeptidase (AEP),[23] is a protease that participates in many physiological and pathological processes,[24] involved in protein turnover for maintenance of homeostasis and protein activation or inactivation for cell signaling,[25] such as antigen processing, cell

[a]*College of Traditional Chinese Medicine, Xinjiang Medical University, Wulumuqi 830011, China. E-mail: wm630@163.com*

[b]*Faculty of Naval Medicine, Second Military Medical University (Naval Medical University), Shanghai 200433, China. E-mail: hormat830713@hotmail.com*

[c]*National Center for Liver Cancer, Shanghai, China, International Co-operation Laboratory on Signal Transduction, Eastern Hepatobiliary Surgery Institute, Second Military Medical University, Shanghai, 200438, China*

[d]*Department of Pharmaceutical Sciences, School of Pharmacy, Second Military Medical University (Naval Medical University), Shanghai 200433, China*

† These authors contributed equally to this work.

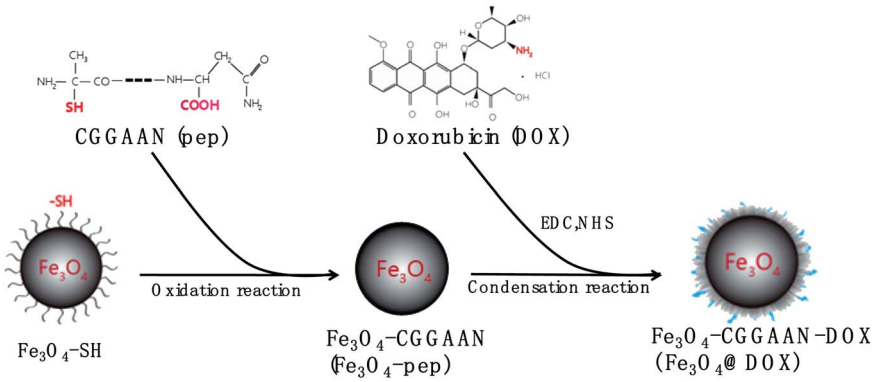

Fig. 1 Schematic illustration of Fe_3O_4@DOX. Fe_3O_4-SH and CGGAAN (pep) were connected through an oxidation reaction to form Fe_3O_4-CGGAAN (Fe_3O_4-pep), of which the carboxyl terminal and the amino group of doxorubicin (DOX) were then condensed to form Fe_3O_4-CGGAAN-DOX (Fe_3O_4@DOX).

migration and proliferation. It specifically recognizes the AAN motif and hydrolyzes proteins or peptide chains from the carboxy terminus of asparagine (Asn). In mammals, LGMN is widely localized to the endolysosome, cell surface, cytosol or nucleus with endopeptidase, carboxy peptidase, and ligase activities.[26,27] Several studies have reported that tumor cells as well as their stromal cells express higher levels of LGMN, thereby exhibiting enhanced migratory and invasive capabilities *via* the activation of pro-MMP2 and cathepsins.[29,30] As the specially recognized motif by LGMN, AAN is a commonly used segment of linked peptide that has widely been used in the field of nanodrug delivery systems with several advantages, including the fast release of target drugs, good biocompatibility, low immunogenicity and no restriction on the size of all substances.[31]

Doxorubicin (DOX) is a highly hydrophilic drug derived by chemical semisynthesis from a bacterial species that is widely used as a chemotherapeutic agent for liver cancer.[32] However, its clinical application is greatly restricted by its strong nonselective cytotoxicity. In terms of the functional properties of the Fe_3O_4 and LGMN, a novel magnetic prodrug Fe_3O_4@DOX was designed and synthesized where Fe_3O_4 and DOX were connected by the designated peptide CGGAAN (Fig. 1). DOX in the magnetic prodrug is supposed to be released from the nanoparticles by LGMN that is usually over-experessed in tumor, thereby reducing its toxicity while maintaining its antagonistic effects on liver cancer.[32,33]

2. Materials and methods

2.1. Chemicals and materials

The reagents and kits commonly used in this study induclude doxorubicin (Solarbio, USA), 1-(3-dimethylaminopropyl)-3-ethylcarbodiimide hydrochloride (Yeyuan Biotech, Shanghai), Fe_3O_4-SH (Ruixi Biotech, Shanxi), *N*-hydroxysuccinimide (Yeyuan Biotech, Shanghai), Anti-LGMN antibody (ABclonal, USA), DMEM medium (Gibco, USA), fetal bovine serum (Gibco, USA), FITC Annexin V Apoptosis Detection Kit with 7-AAD (BioLegend, USA), and TUNEL Apoptosis Kit (RuiBo, Shanghai). The PGMLV-CMV-H_LGMN-3 × Flag-EF1-ZsGreen1-T2A-Puro plasmid was constructed by Jiman Biological Company (Shanghai, CN). Human liver cancer cells (PLCs) were kindly provided by National Liver Cancer Science Center of China (Shanghai, CN). BABL/c male nude mice were purchased from the Animal Experimental Center of Naval Military Medical University (Shanghai, CN). All animal procedures were performed in accordance with the Guidelines for Care and Use of Laboratory Animals of "Naval Military Medical" University and approved by the Animal Ethics Committee of "Naval Military Medical.

2.2. Fe_3O_4@DOX synthesis

The Fe_3O_4-pep (Fe_3O_4-CGGAAN) particles were first synthesized by mixing with 5 mg mL^{-1} of Fe_3O_4-SH (Rui Xi Inc., China) with the linked peptide CGGAAN (1, 2.5, 5, and 10 mg) to a final volume : mass ratio of 1 : 1, 1 : 2.5, 1 : 5 or 1 : 10 at room temperature for 2 h. The unconjugated polypeptides were removed by dialysis overnight. After screening the particle size and homogeneity, the 1 : 2.5. The Fe_3O_4-pep sample (1 mL) was ultrasonically dispersed into 5 mL of 4-morpholineethanesulfonic acid hydrate buffer (0.01 M, pH 6.0), followed by the addition of 40 mg of 1-(3-dimethylaminopropyl)-3-ethylcarbodiimide hydrochloride (EDC) and 60 mg of *N*-hydroxysuccinimide (NHS) at room temperature, playing roles in protecting and re-activating the carboxyl group, respectively. The solution was then ultrasonicated for 15 s, shaken at 37 °C for 15 min, and centrifuged at 12 000 × *g* for 10 min. The pellets were resuspended in 5 mL of PBS solution with 5 mg mL^{-1} DOX, rapidly sonicated for 30 s, and shaken at 37 °C overnight. The synthesized Fe_3O_4@DOX samples were centrifuged, washed three times, and resuspended in 4.5 mL of PBS. Finally, the coupling rate of DOX was calculated under the standard curve of DOX established by measuring the absorbance at 485 nm with a microplate reader. The formula is as follows: coupling rate (%) = $100 \times (m_{\text{amount of drug invested}} - m_{\text{free drug}})/m_{\text{amount of drug invested}}$.

2.3. Characterization of the magnetic nanoparticles

The relationship between the standing time and the precipitation of Fe_3O_4-pep with different volume : mass ratios was first compared by determining the precipitation (%) and turbidity (%) with naked eyes, where the samples with full of diaphaneity

were considered as 100% precipitation and 0% turbidity while the solutions were homogeneous without any precipitation were recognized as 0% precipitation and 100% turbidity. Then, the morphologies and particle sizes were observed by transmission electron microscopy (TEM, JEOL-1230, Japan) 1–2 weeks after particle synthesis. The particle solutions were blended before the preparation of TEM samples. The particle size was tested by the TEM automatic image analysis software whereas the ratio of dispersity was also calculated by counting the adhesive particles. Then, the optimal ratio of 1 : 2.5 Fe_3O_4-pep particles were selected to further test the size and zeta potential with a Malvern Zetasizer instrument (Malvern Zetasizer Nano ZS, UK). The disulfide bond between Fe_3O_4-SH and CGGAAN was confirmed by Raman spectroscopy (Renishaw, in Via, UK), whereas the specific bonds, including Fe–O, C–H, C=O and O–H, were observed by Fourier transform infrared spectroscopy (FT-IR, MEXUS, USA). After coupling Fe_3O_4-SH with CGGAAN, X-ray diffraction (XRD, Kratos, Japan) was used to detect whether crystal form was changed. In addition to transmission electron microscopy and the Malvern Zetasizer instrument, which were utilized to test the morphology, size and zeta potential, the fluorescence spectrum of Fe_3O_4@DOX was screened by a fluorophotometer (Thermo Fisher, Lumina, USA).

2.4. Construction of the LGMN-overexpressing lentivirus

The target LGMN gene was first amplified by polymerase chain reaction (PCR) from the original pUC57 plasmid that contains only the LGMN sequence with the sense primer 5′-GCGAATTCGAAGTA-TACCTCGAGGCCACCATGGTTTGGAAAGTAGCTGTATTCCT-3′ and antisense primer 3′-GTCATGGTCTTTGTAGTCGGATCCG-TAGTGACCAAGGCACACGTG-5′. The LGMN segment was inserted into the plasmid PGMLV-CMV through a specific digestion site (XhoI and BamHI) contained at both ends of the primers to construct the overexpression core plasmid PGMLV-CMV-H_LGMN-3 × Flag-EF1-ZsGreen1-T2A-Puro of the lentivirus, which was then cotransfected with three auxiliary packaging plasmids, VSV-G, GAG, and REV, into HEK293T cells with the HG transfection reagent. Enhancing buffer was added after 10–12 h of transfection and changed to fresh medium after 8 h. After 48 h of incubation, the supernatants of the cells enriched with the lentivirus particles were collected. The obtained viruses were verified by fluorescence microscopy (Olympus Co., Japan) and western blot analysis.

2.5. Construction of stable LGMN-overexpressing PLCs

PLCs obtained from the Naval Medical University (Shanghai, China) were incubated in DMEM containing 10% fetal bovine serum (FBS) and 1% penicillin/streptomycin, in a 5% CO_2 incubator at 37 °C. Stable LGMN-overexpressing PLCs were constructed through transfection with the successfully constructed lentivirus carrying the LGMN segment. Briefly, the negative control (NC) lentivirus at a final titer of 16×10^6 TU per mL (transfection unit) and a series of LGMN-overexpressing lentiviruses to final titers of 4×10^6, 8×10^6, 12×10^6 and 16×10^6 TU per mL were added to different six-well dishes that were plated with PLCs at the same density of 3×10^5 cells per mL. Polybrene (10 μg mL^{-1}) was also added to improve the infection efficiency on the following day. After 24 h, puromycin (0.5 μg mL^{-1}) was added and changed once every two days for a period of 15 days. The treated cells (Olympus Co, Japan) were observed with a fluorescence microscope, and the expression of LGMN was verified by western blot analysis.

2.6. Western blot analysis

PLCs with and without overexpressing LGMN at the same density of 2×10^6 cells per mL were seeded and cultured for 24 h in 10 cm dishes (Corning Inc, NY, USA). The cells were harvested in RIPA lysis buffer (Beyotime), and the total protein was quantitated with the BCA assay (Thermo Fisher, USA). The protein samples (30 μg per well) were loaded and separated by 12% SDS-PAGE and transferred to a nitrocellulose filter membrane at 230 mA for 72 min. After blocking with 5% skimmed milk powder, it was incubated with the primary antibody (1 : 1000) at 4 °C overnight and then with the secondary antibody (1 : 1000). The complexes were detected by enhanced chemiluminescence (ECL, 4A Biotech Co, Shanghai) and visualized using ChemiDoc XRS (Bio-Rad, USA). The intensity of the band for each protein was normalized to the internal reference GAPDH.

2.7. Cellular uptake

LGMN-overexpressing PLCs at a density of 5×10^3 cells per well were first plated in six-well plates overnight. After the cells were successfully attached, DOX and Fe_3O_4@DOX at the same final concentration of 10 μg mL^{-1} were added for 0, 0.5, 1 and 3 h. The DOX fluorescence in each well was observed by confocal laser scanning microscopy (Zeiss LSM 710, Germany) with excitation and emission wavelengths of 485 nm and 585 nm, respectively.

2.8. Cytotoxicity and apoptosis

After the PLCs with or without LGMN overexpression were attached at a density of 5×10^3 cells per well, different concentrations of free DOX and Fe_3O_4@DOX were added to the well at a final volume of 100 μL and then incubated at 37 °C and 5% CO_2 for 24 h. Then, MTT solution (20 μL, 5 mg mL^{-1}) was added, and the incubation was continued for another 4 h. After removing the culture solution, 200 μL of dimethyl sulfoxide was added to each well, and the plates were shaken at a low speed for 10 s to fully dissolve the crystals. The absorbance was finally measured at 480 nm.

The LGMN-overexpressing PLCs were seeded in six-well plates at a density of 2×10^5 cells per well in 2 mL of complete DMEM and cultured for 24 h for attachment. The medium was then removed and replaced by fresh medium containing free DOX (10 μg mL^{-1}) or Fe_3O_4@DOX (containing DOX 10 μg mL^{-1}) and incubated for 24 h. The treated cells were collected and washed three times with ice-cold PBS and stained with FITC-Annexin V and 7-amino-actinomycin D (7-AAD). Quantitative measurements of apoptosis and necrosis were performed by flow cytometry (BD FACS Calibur, USA).

2.9. *In vivo* antitumor assessment

After resuspension in a mixture of matrigel (Corning Inc., NY, USA) and DMEM (v/v = 1/9), the cultured PLCs (0.1 mL, 1×10^7 cells per mL) were injected into the subcutaneous part of the left thigh to produce the liver cancer model in nude mice. When the tumor volume reached approximately 130 mm^3, the nude mice were randomly divided into four groups ($n = 6$). Free DOX (5 mg kg^{-1}), Fe_3O_4@DOX (containing 5 mg kg^{-1} DOX) and equivalent amounts of Fe_3O_4-SH and PBS were then administered intravenously every other day for a total of ten days. During this period, the mouse weights and tumor sizes were measured with a Vernier caliper. The tumor volumes were calculated by the equation: volume $= 0.5 \times L \times W^2$, where L and W represent the length and width of the tumor, respectively. At the same time, the time to death of each mouse was recorded, and a survival curve was drawn. The mice were then sacrificed, and the tumors and livers were extracted. Liver and tumor tissues in the PBS group were taken to verify the expression of legumain. Hematoxylin and eosin staining (H&E) was performed on paraffin sections of the tumors. In addition, paraffin sections of the tumors were subjected to terminal deoxynucleotidyl transferase dUTP nick end labeling (TUNEL) staining.

2.10. Statistical analysis

Values are represented as the mean ± standard deviation. Student's *t*-test between two groups and ANOVA among multiple groups were used to evaluate the statistical significance of differences by the Sofare GraphPad Prism 8.0.2. Data were considered statistically significant at $*p < 0.05$, $**p < 0.01$.

3. Results

3.1. Construction of Fe_3O_4@DOX and its characterization

Using the sulfhydryl nanoparticle Fe_3O_4-SH, we first synthesized a series of Fe_3O_4-CGGAAN (Fe_3O_4-pep) with different mass ratios of Fe_3O_4-SH to CGGAAN (1 : 1, 1 : 2.5, 1 : 5 and 1 : 10). Under standing conditions, the Fe_3O_4-peps produced dose-dependent and time-dependent precipitation, where the 1 : 1 and 1 : 2.5 Fe_3O_4-peps were evenly dispersed after 24 h, which was similar to that of the blank Fe_3O_4-SH, while the 1 : 5 and 1 : 10 Fe_3O_4-pep solutions showed substantial precipitation after 24 h and their supernatants became obviously transparent (Fig. 2A).

Then, the morphologies and particle sizes of the Fe_3O_4-peps were investigated by TEM (Fig. 2B). All the Fe_3O_4-peps were circular, and the particle sizes increased from less than 60 nm for Fe_3O_4-SH to approximately 120 nm for 1 : 10 Fe_3O_4-pep. The Fe_3O_4-peps tended to adhere and agglomerate, and the sample dispersity (%) decreased dose-dependently (Fig. 2C). Similar results were obtained by using a Malvern Zetasizer instrument, in which the average particle sizes obtained ranged from 83.5 nm in Fe_3O_4-SH to 231 nm in Fe_3O_4-pep with a ratio of 1 : 2.5 (Fig. 2E); the larger sizes measured compared with those by TEM can be reasonably attributed to the adhesion and

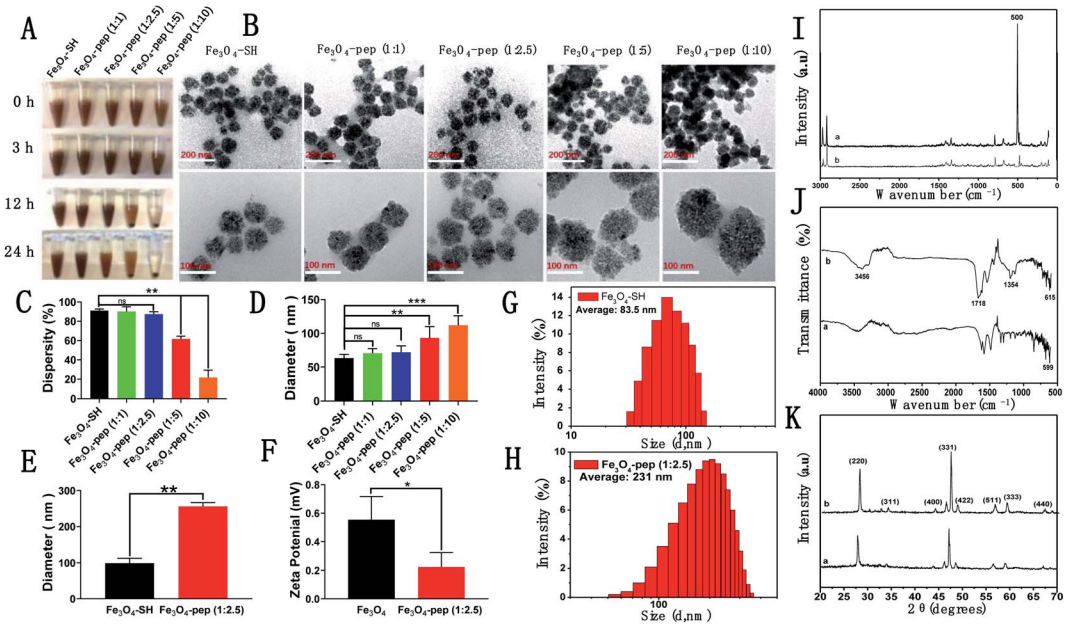

Fig. 2 Screening of Fe_3O_4-pep and its characterization. (A) The precipitation map of Fe_3O_4-pep with different doses of the peptide CGGAAN over 24 h. (B) Representative TEM images. (C) Dispersity of Fe_3O_4-pep with different CGGAAN doses. (D) Diameter of Fe_3O_4-pep with different CGGAAN doses. (E) Representative Fe_3O_4-SH particle size chart from a Malvern particle size analyzer. (F) Representative 1 : 2.5 Fe_3O_4-pep particle size chart from a Malvern particle size analyzer. (G) Statistics of the particle sizes of Fe_3O_4-SH and 1 : 2.5 Fe_3O_4-pep. (H) Statistics of the zeta potentials of Fe_3O_4-SH and 1 : 2.5 Fe_3O_4-pep. (I) Raman spectrum of diffraction of Fe_3O_4-SH (a) and 1 : 2.5 Fe_3O_4-pep (b). (J) Fourier transform infrared spectra of Fe_3O_4-SH (a) and 1 : 2.5 Fe_3O_4-pep (b). (K) X-ray diffraction of Fe_3O_4-SH (a) and 1 : 2.5 Fe_3O_4-pep (b). $n = 3$; ns, not significant; $*p < 0.05$; $**p < 0.01$.

agglomeration tendencies that were supported by the zeta potential that decreased from 0.628 mV to 0.266 mV (Fig. 2F). Additionally, the S–S stretching between Fe_3O_4-SH and CGGAAN was successfully confirmed with the obvious absorption peak at approximately 500 cm^{-1} in the Raman spectrum of the sample Fe_3O_4-pep (Fig. 2I). Similarly, CGGAAN contains cysteine, glycine, alanine and asparaginate, significant variations in the absorption peaks V_{max}/cm^{-1} 615 (FeO), 1354 (CH), 1718 (CO), and 3456 (OH) from Fourier transform infrared spectroscopy (FT-IR) measurements (Fig. 2J) indicated the successful synthesis of Fe_3O_4-pep by the connection between Fe_3O_4-SH and CGGAAN.[24] The structure and chemical composition of Fe_3O_4-SH and Fe_3O_4-peps were revealed from the XRD analysis (Fig. 2K), where the peaks of both samples were indexed to the 220, 311, 400, 331, 422, 511, 440, and 533 planes, which are attributed to the 2θ of 30.46°, 35.76°, 43.51°, 56.69°, 53.24°, 56.88°, 63.32°, and 71.41°, respectively, with the standard diffraction spectrum (ref. code Fe_3O_4: 01-088-0315),[34] indicating no phase change of Fe_3O_4 by the conjugation of the polypeptide CGGAAN.

After the connection of DOX to Fe_3O_4-CGGAAN, the diameter of the synthesized Fe_3O_4@DOX by TEM was 95 nm (Fig. 3A), which was much smaller than the 322.5 nm (Fig. 3C) measured by the Malvern Zetasizer instrument. This difference can also be explained by the existence of partial adhesion and the appearance of white flocculent substances on the surface of the nanoparticles (Fig. 3A). The spontaneous fluorescence spectrum of DOX was also scanned, and the maximal emission wavelength of DOX was obviously right-shifted from 550 nm for free DOX to 615 nm in the synthesized Fe_3O_4@DOX without any change in the wave width, implying that DOX was successfully coupled to the Fe_3O_4-pep particles (Fig. 3E–G). Moreover, the coupling rate of 85% was obtained by calculating the variation in the fluorescence intensity of the free DOX before and after coupling.

3.2. Construction of LGMN-overexpressing PLCs

Previous studies have reported that the expression level of LGMN in PLCs is not high when compared with the high expression of LGMN in tumor tissues, therefore, a PLC cell line with a stable and high expression level of LGMN was constructed by using lentivirus infection to assess the *in vitro* effects of Fe_3O_4@DOX on tumor cells. The LGMN-overexpressing lentivirus was successfully constructed and harvested with a titer of 5×10^8 TU per mL by cotransfection of the core plasmid PGMLV-CMV-H_LGMN-3 × Flag-EF1-ZsGreen1-T2A-Puro expressing LGMN-GFP and three helper plasmids (VSV-G, GAG, and REV) in HEK293T cells. Then,

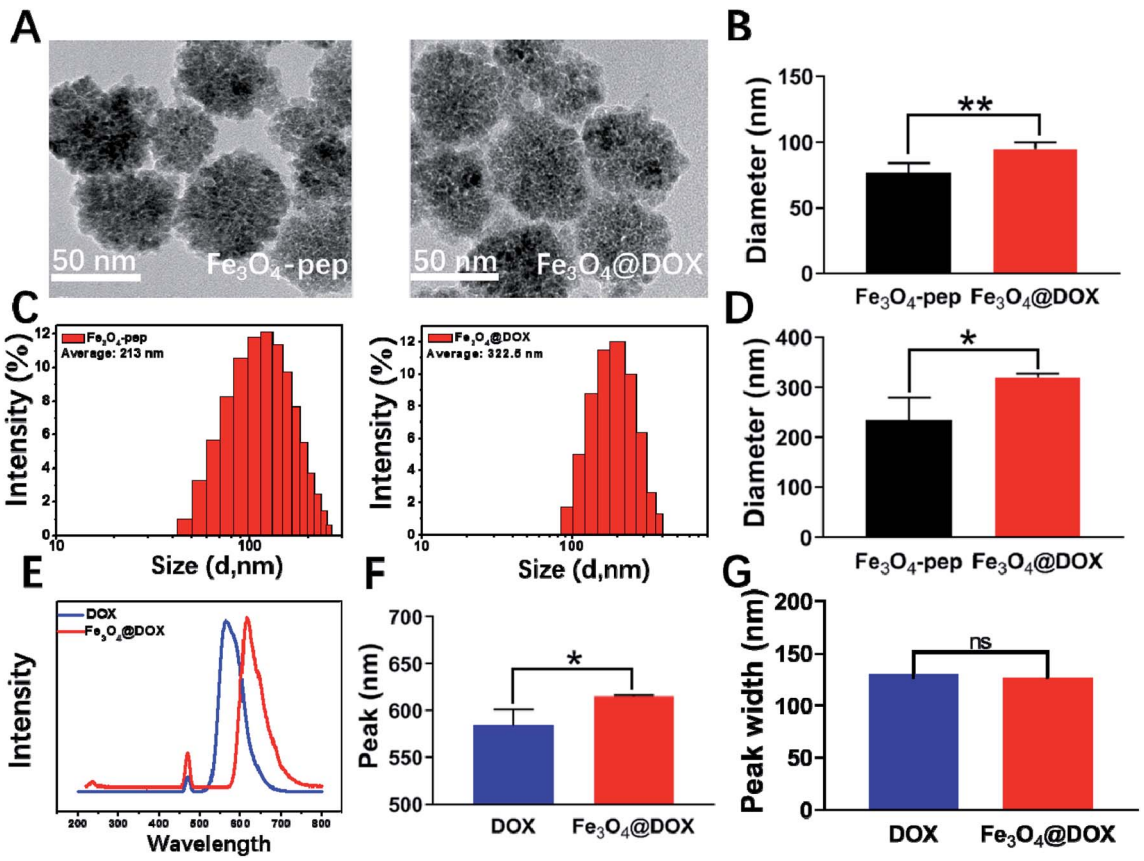

Fig. 3 Synthesis and characterization of Fe_3O_4@DOX. (A) Representative TEM images of Fe_3O_4-pep and Fe_3O_4@DOX. (B) Statistics of the particle sizes of Fe_3O_4-SH and Fe_3O_4-pep by TEM. (C) Typical particle size diagram of Fe_3O_4-pep and Fe_3O_4@DOX. (D) Statistics of particle size for Fe_3O_4-SH and Fe_3O_4-pep from a Malvern particle size analyzer. (E) Fluorescence emission spectra of free DOX and Fe_3O_4@DOX. (F) The peak emission wavelengths of free DOX and Fe_3O_4@DOX. (G) The peak widths of free DOX and Fe_3O_4@DOX. $n = 3$; ns, not significant; *$p < 0.05$; **$p < 0.01$.

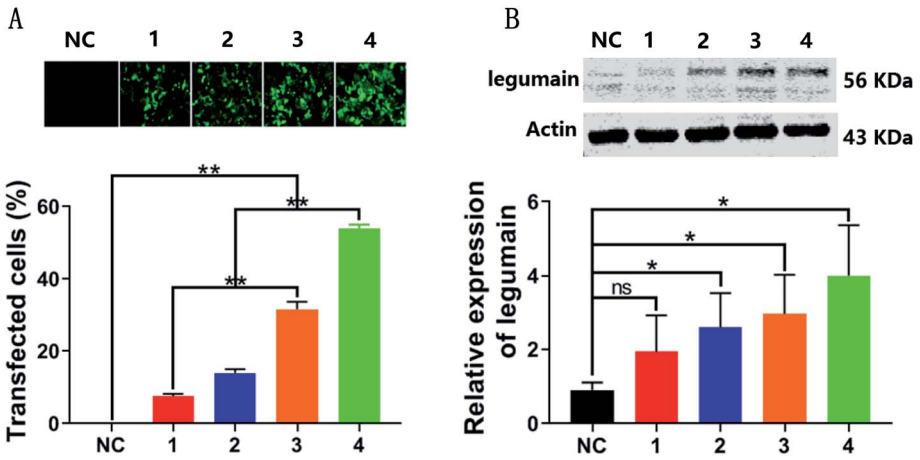

Fig. 4 The construction and evaluation of LGMN-overexpressing PLCs. (A) The fluorescence intensity of LGMN-overexpressing PLCs. (B) Western blot analysis was used to verify the expression of LGMN. NC, 1, 2, 3 and 4 represent the negative control with a blank plasmid titer of 16×10^6 TU per mL, LGMN-overexpression lentivirus 4×10^6, 8×10^6, 12×10^6 and 16×10^6 TU per mL, respectively. $n = 3$; ns, not significant; *$p < 0.05$; **$p < 0.01$.

the PLCs were infected with lentivirus at a series of diluted titers of 4×10^6, 8×10^6, 12×10^6 and 16×10^6 TU per mL. After 15 days of screening with puromycin, four PLCs stably expressing LGMN were obtained where both GFP and LGMN increased dose-dependently. Among them, the number of GFPs in PLCs infected with lentivirus at a titer of 16×10^6 TU per mL reached a maximum of 50%, which was almost 10 times that of the PLCs with the lowest lentivirus titer of 4×10^6 TU per mL. The expression of LGMN was directly proportional to the lentiviral titer of PLCs infected and the expression of LGMN in the control group was very low, which was consistent with previous reports.[26] The relative expression of LGMN in PLCs with a lentivirus titer of 16×10^6 TU per mL was approximately 4 times that of negative control. Therefore, we successfully constructed several LGMN-overexpressing PLCs, of which the cell line with the maximum lentiviral titer of 16×10^6 TU per mL was used for subsequent cell uptake and cytotoxicity studies (Fig. 4).

3.3. Cellular uptake

Using the method of scanning the autofluorescence of DOX by laser confocal microscopy, we comparatively studied the cellular uptake of free DOX and Fe_3O_4@DOX in LGMN-overexpressing PLCs. Free DOX was able to quickly enter LGMN-overexpressing PLCs, approached saturation at approximately 1 h (Fig. 5A), and a high level was maintained for 3 h. In contrast, the entry of DOX from Fe_3O_4@DOX into cells can be divided into two distinct stages, the fast entry period within 1 h followed by a slow entry period between 1–3 h. Although it is called the fast entry period within 1 h, the speed of DOX from Fe_3O_4@DOX was much slower than that of free DOX, which is probably due to the slow process of Fe_3O_4@DOX entering into the cells. After another 2 h of the slow entry period, the amount of intracellular DOX from Fe_3O_4@DOX in LGMN-overexpressing PLCs was close to that in the free DOX group. In short, Fe_3O_4@DOX significantly delays the entry of DOX into the cells and has an obvious slow-release effect.

3.4. *In vitro* cytotoxicity and cell apoptosis

We further studied the cytotoxic effects of free DOX and Fe_3O_4@DOX on both PLCs and LGMN-overexpressing PLCs using the 3-(4,5-dimethylthiazol-2-yl)-2,5-diphenyltetrazolium bromide (MTT) method. In the range of 10^{-5} to 100 μg mL^{-1},

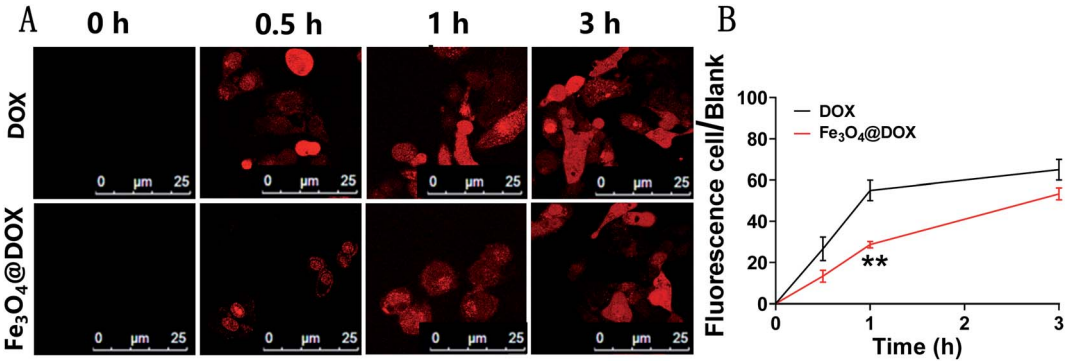

Fig. 5 Confocal laser scanning of DOX autofluorescence in LGMN-overexpressing PLCs after treatment with free DOX (10 μg mL^{-1}) and Fe_3O_4@DOX (containing 10 μg mL^{-1} DOX) for 0 h, 0.5 h, 1 h and 3 h. (A) Typical images and (B) statistics of fluorescence to fluorescent cells. $n = 3$; ns, not significant; *$p < 0.05$; **$p < 0.01$.

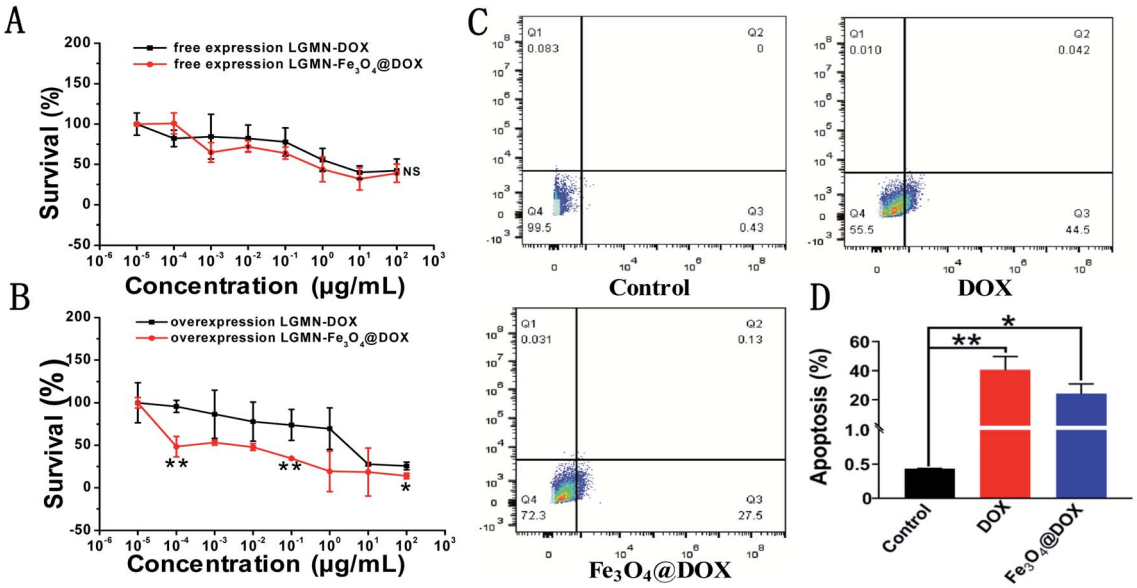

Fig. 6 *In vitro* cytotoxicity and cell apoptosis. (A) Cytotoxicity of DOX and Fe_3O_4@DOX on PLCs. (B) Cytotoxicity of DOX and Fe_3O_4@DOX on LGMN-overexpressing PLCs ($n = 6$). (C) Typical flow cytometry graphs after treatment with PBS, DOX and Fe_3O_4@DOX in LGMN-overexpressing PLCs. (D) Statistics of flow cytometry after treatment with PBS, DOX and Fe_3O_4@DOX in LGMN-overexpressing PLCs. *$p < 0.05$; **$p < 0.01$.

we observed that free DOX and Fe_3O_4@DOX can produce significant toxic effects on both PLCs and LGMN-overexpressing PLCs. Among them, free DOX and Fe_3O_4@DOX showed considerable toxic effects on PLCs at various concentrations, and there was no significant difference between the two groups (Fig. 6A). In LGMN-overexpressing PLCs, Fe_3O_4@DOX had a stronger killing effect, especially at low concentrations of 10^{-5} to 1 μg mL^{-1}, with significant differences (Fig. 6B). The stronger cytotoxicity is probably related to the fact that Fe_3O_4@DOX is more likely to accumulate in cells by endocytosis, magnetic

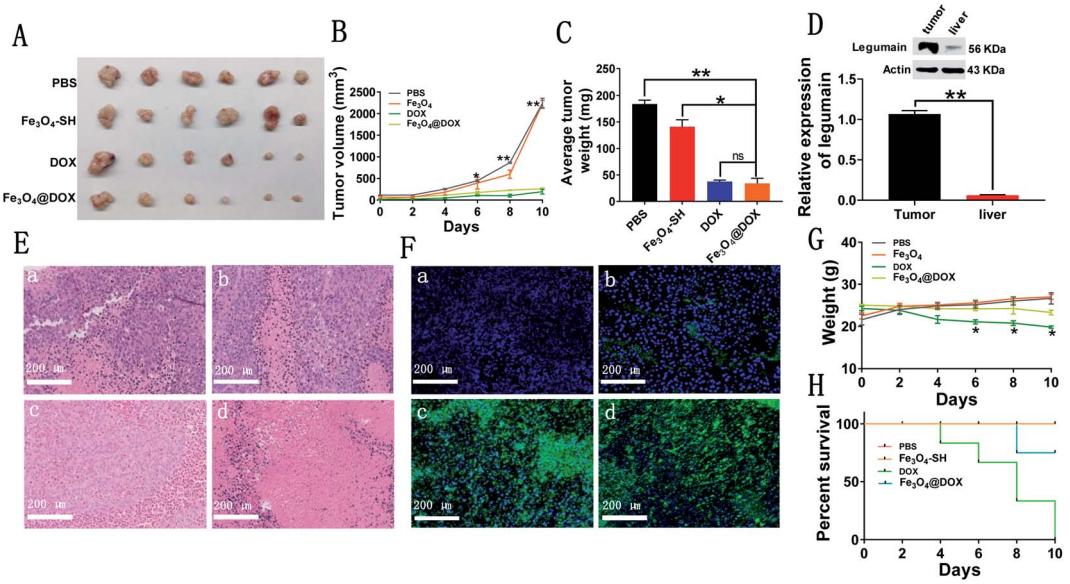

Fig. 7 *In vivo* tumoricidal effect of Fe_3O_4@DOX. (A) Tumor pictures extracted from nude mice after administration with PBS, Fe_3O_4, DOX (5 mg kg^{-1}) and Fe_3O_4@DOX (containing 5 mg kg^{-1}). (B) The volume change of the tumor after administration with PBS, Fe_3O_4, DOX (5 mg kg^{-1}) and Fe_3O_4@DOX (containing 5 mg kg^{-1}). $n = 6$. (C) The average weight of subcutaneous liver tumors after the intervention period of 10 days. $n = 6$. (D) Western blot of LGMN from the tumor and liver tissue in nude mice. $n = 3$. (E) H&E staining of tumor tissue (magnifications, ×200) after administration with PBS, Fe_3O_4, DOX (5 mg kg^{-1}) and Fe_3O_4@DOX (containing 5 mg kg^{-1}). $n = 3$. (F) TUNEL staining of tumor tissue (magnifications, ×200) after administration with PBS, Fe_3O_4, DOX (5 mg kg^{-1}) and Fe_3O_4@DOX (containing 5 mg kg^{-1}). $n = 3$. (G) Changes of body weight of nude mice after administration with PBS, Fe_3O_4, DOX (5 mg kg^{-1}) and Fe_3O_4@DOX (containing 5 mg kg^{-1}), $n = 6$. (H) Survival curves of nude mice after administration with PBS, Fe_3O_4, DOX (5 mg kg^{-1}) and Fe_3O_4@DOX (containing 5 mg kg^{-1}), $n = 6$. *$p < 0.05$; **$p < 0.01$.

targeting and natural settlement. We further tested the effects of free DOX and Fe_3O_4@DOX on cells by flow cytometry and found that both free DOX and Fe_3O_4@DOX at the same concentration of 10 μg mL^{-1} can significantly induce apoptosis in LGMN-overexpressing PLCs rather than necrosis (Fig. 6C and D), which is consistent with previous reports.

3.5. *In vivo* antitumor assessment of Fe_3O_4@DOX

Finally, we implanted PLCs subcutaneously in the left lower extremity of nude mice and successfully generated subcutaneous liver tumor models, which were further used to evaluate the *in vivo* effects of free DOX and Fe_3O_4@DOX on liver cancer in nude mice. When the subcutaneous liver tumor grew to approximately 130 mm^3, we injected PBS, Fe_3O_4-SH, free DOX or Fe_3O_4@DOX into the each group every two days. Compared with the PBS and Fe_3O_4-SH groups, free DOX and Fe_3O_4@DOX at the same DOX dose of 5 mg kg^{-1} *i.v.* significantly inhibited the growth of the subcutaneous liver tumor volume (Fig. 7A and B). After the administration period of 10 days, we sacrificed the mice and found that the tumors in the free DOX and Fe_3O_4@DOX groups were significantly smaller and lighter than those in the PBS and Fe_3O_4-SH groups, and there was no significant difference between the two groups (Fig. 7C). We also confirmed the increase in LGMN in the subcutaneous liver tumor tissues compared with liver tissues by western blot (Fig. 7D). In addition, H&E staining showed that the number of tumor cells in the tumor tissues treated with free DOX and Fe_3O_4@DOX significantly decreased, whereas the number of dead cells significantly increased (Fig. 7E). TUNEL staining showed that the number of apoptotic cells in tumor tissues increased significantly after treatment with free DOX and Fe_3O_4@DOX (Fig. 7F), which is consistent with the results from the *in vitro* flow cytometric experiments. Remarkably, the weights of the nude mice after treatment with free DOX were much lighter than those with Fe_3O_4@DOX treatment, and all the tested mice were dead within 10 days in the free DOX-treated group; only one mouse died after treatment with Fe_3O_4@DOX at the same dose of 5 mg kg^{-1} *i.v.* All the results indicated that Fe_3O_4@DOX maintains an equal antagonistic effect to free DOX on subcutaneous liver tumors but significantly reduces the *in vivo* toxicity of DOX.

4. Discussion

Frontier nanobiotechnology research confirms that nanomedicine carriers have great potential for drug delivery, targeted diagnosis, and treatment of cancer.[27,35–37] In this study, we produced the magnetic nanoparticle Fe_3O_4@DOX with three functional elements, Fe_3O_4-SH, CGGAAN and DOX. Fe_3O_4-SH is the core magnetic nanoparticle with a diameter of approximate 60 nm as tested by TEM, which has the potential to take drugs to the tumor tissue through the EPR effect and to further enter the cells through endocytosis.[38–40] For instances, a multifunctional Janus nanocomposite M-MSNs-DOX was previously engineered with a head of magnetic Fe_3O_4 and a body of mesoporous SiO_2 containing DOX as 'nano-bullets', which was determined to induce selective growth inhibition to the cancer cell under magnetic field rather than human normal cells due to its preferable endocytosis by the tumor cells and pH-promoted DOX release in the interior of cancer cells. Park B. J. *et al.*, acquired *in vitro* MR images of cancer cells (PC-3) and confirmed the good biocompatibility of another magnetic nanoparticle $CoFe_2O_4$@HP in both normal and cancer cells, and its potential as an agent for photodynamic therapy (PDT).[28] CGGAAN is the short connective peptide between the magnetic particle Fe_3O_4-SH and the effective antagonistic drug DOX. The AAN motif can be specifically recognized and cut by LGMN, which is highly expressed in solid tumors but not normal tissues. The connection of antitumor drugs to AAN can be specifically cleaved, thereby releasing the drug to kill the tumor.[41] Cheng L. *et al.* used the AAN motif to chemically couple with DOX as a legubicin prodrug, which was proven to reduce the side effects of DOX and to enhance its antitumor effects.[29]

The diameter of the synthesized Fe_3O_4@DOX was 95 nm as tested by TEM. The larger size of 322.5 nm tested by the Malvern

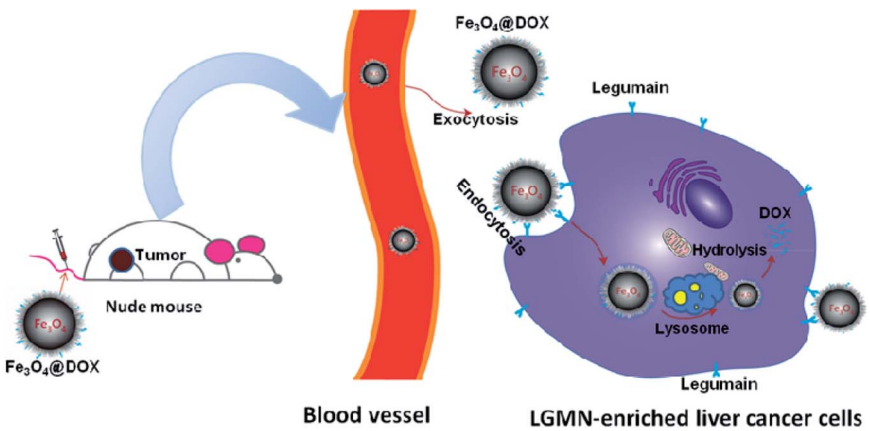

Fig. 8 Schematic illustration of the mechanism of tumor delivery by Fe_3O_4@DOX. After the intravenous injection of Fe_3O_4@DOX, the magnetic particles reach the tumor through the EPR effect and enter the tumor cells by endocytosis. DOX in Fe_3O_4@DOX is released by both the extracellular and intracellular LGMN that is highly expressed in solid tumor, thereby playing the antagonistic effect on liver cancer by inducing cell apoptosis.

Zetasizer instrument is probably because of the partial adhesion to form tiny unstable particles that cannot be distinguished with naked eyes. XRD is a widely used technique to analyze the crystalline/amorphous nature of nanoparticles along with its phase and purity of sample, in our study, there was no distinct change in structure of Fe_3O_4@DOX before and after being coupled with CGGAA.[30,42] By using LGMN-overexpressing PLCs, we found that Fe_3O_4@DOX has a slow-release effect, where the entry of DOX from Fe_3O_4@DOX into cells is much slower than that of free DOX, which can be easily explained by the process of endocytosis and is specifically cut by LGMN. Moreover, the *in vitro* MTT and flow cytometric experiments showed that Fe_3O_4@DOX can induce similar cell apoptosis to that of free DOX and has more sensitive toxicity to PLCs at low DOX concentrations, indicating the maintenance of DOX cytotoxicity and magnetic targeting. The most important results came from the *in vivo* antitumor assessment, where Fe_3O_4@DOX maintains an equal antagonistic effect to free DOX on subcutaneous liver tumors but significantly reduces the *in vivo* toxicity of DOX.

Eva K. Schlachter *et al.*, used Magnetic Resonance Imaging Technology to evaluate the *in vivo* degradation of iron oxide magnetic nanoparticle patches, and carried out iron content localization and biodistribution. None of the histological examinations showed that the ferromagnetic nanoparticles degraded or aggregated outside the reticuloendothelial system. TEM observed local uptake of ferromagnetic nanoparticles by macrophages and reticuloendothelial cells. Apoptosis staining of caspase cells showed no significant increase in toxicity. The ferromagnetic nanoparticle patch in animals is relatively inert within 6 months, and local degradation is slow. No distant structural changes were observed in the tissues studied. Therefore, Fe_3O_4 used in this study is predicted to be of low toxicity and has no effect on the use of Fe_3O_4@DOX as the ferromagnetic DOX carrier.

All the above investigations draw the conclusion that we have successfully synthesized a novel magnetic nanoparticle Fe_3O_4@DOX that maintains the antagonistic effects of DOX on a subcutaneous liver cancer model while reducing the *in vivo* toxicity. The inhibitory process is hypothesized as follows (Fig. 8). When intravenous Fe_3O_4@DOX reach the tumor and contact the liver tumor cells through the EPR effect in nude mice, the AAN motif in Fe_3O_4@DOX will first be recognized and cut by the LGMN on the surface of the tumor or cells, thereby releasing DOX to start the effect of killing tumor cells. Meanwhile, the unreleased DOX in Fe_3O_4@DOX will then enter the tumor cells through endocytosis, and be released by intracellular LGMN to further kill the tumor cells. Because the Fe_3O_4@DOX can accumulate in tumor through the EPR effect and the LGMN is highly expressed in solid tumor than that in normal tissues, DOX in Fe_3O_4@DOX is supposed to be specifically targeted to the solid tumor and therefore reduces the *in vivo* toxicity while maintains its antagonistic effects. In an all, we have successfully synthesized the magnetic nanoparticle Fe_3O_4@DOX as a promising prodrug of DOX for liver cancer treatment.

Conflicts of interest

The authors declare no conflicts of interest.

Acknowledgements

This work was supported by the Regional Science Foundation (2017D01C207).

References

1 L. Che, M. G. Pilo, A. Cigliano, G. Latte, M. M. Simile, S. Ribback, F. Dombrowski, M. Evert, X. Chen and D. F. Calvisi, *Cell Cycle*, 2017, **16**, 499–507.
2 J. A. Gingold, D. Zhu, D. F. Lee, A. Kaseb and J. Chen, *Trends Mol. Med.*, 2018, **24**, 395–411.
3 L. A. Torre, F. Bray, R. L. Siegel, J. Ferlay, J. Lortet-Tieulent and A. Jemal, *Ca-Cancer J. Clin.*, 2015, **65**, 87–108.
4 F. Bray, J. Ferlay, I. Soerjomataram, R. L. Siegel, L. A. Torre and A. Jemal, *Ca-Cancer J. Clin.*, 2018, **68**, 394–424.
5 K. N. Lokesh, T. Chaudhuri, K. C. Lakshmaiah, K. G. Babu, L. Dasappa, L. A. Jacob, M. C. Suresh Babu, A. H. Rudresha and L. K. Rajeev, *Indian J. Cancer*, 2017, **54**, 526–529.
6 J. Ferlay, I. Soerjomataram, R. Dikshit, S. Eser, C. Mathers, M. Rebelo, D. M. Parkin, D. Forman and F. Bray, *Int. J. Cancer*, 2015, **136**, E359–E386.
7 I. Labgaa, N. Demartines and E. Melloul, *Hepatology*, 2019, **69**, 923.
8 S. Mura, J. Nicolas and P. Couvreur, *Nat. Mater.*, 2013, **12**, 991–1003.
9 O. Tredan, C. M. Galmarini, K. Patel and I. F. Tannock, *J. Natl. Cancer Inst.*, 2007, **99**, 1441–1454.
10 P. C. Lyon, M. D. Gray, C. Mannaris, L. K. Folkes, M. Stratford, L. Campo, D. Y. F. Chung, S. Scott, M. Anderson, R. Goldin, R. Carlisle, F. Wu, M. R. Middleton, F. V. Gleeson and C. C. Coussios, *Lancet Oncol.*, 2018, **19**, 1027–1039.
11 H. Cabral, K. Miyata, K. Osada and K. Kataoka, *Chem. Rev.*, 2018, **118**, 6844–6892.
12 K. Prusty and S. K. Swain, *Int. J. Biol. Macromol.*, 2019, **126**, 765–775.
13 C. Ash, G. Town, R. Whittall, L. Tooze and J. Phillips, *Lasers Med. Sci.*, 2017, **32**, 1927–1933.
14 H. J. Lee and Y. Y. Lee, *Pharmazie*, 2010, **65**, 520–522.
15 X. Chen, L. Tan, T. Liu and X. Meng, *Curr. Drug Delivery*, 2017, **14**, 307–322.
16 S. Kwiatkowski, B. Knap, D. Przystupski, J. Saczko, E. Kedzierska, K. Knap-Czop, J. Kotlinska, O. Michel, K. Kotowski and J. Kulbacka, *Biomed. Pharmacother.*, 2018, **106**, 1098–1107.
17 J. L. Corchero and A. Villaverde, *Trends Biotechnol.*, 2009, **27**, 468–476.
18 C. Shen, X. Wang, Z. Zheng, C. Gao, X. Chen, S. Zhao and Z. Dai, *Int. J. Nanomed.*, 2019, **14**, 101–117.
19 L. Mohammed, D. Ragab and H. Gomaa, *Curr. Pharm. Des.*, 2016, **22**, 3332–3352.

20 P. A. Kotelnikova, V. O. Shipunova, U. F. Aghayeva, O. A. Stremovskiy, M. P. Nikitin, I. A. Novikov, A. A. Schulga, S. M. Deyev and R. V. Petrov, *Dokl. Biochem. Biophys.*, 2018, **481**, 198–200.
21 R. Hao, R. Xing, Z. Xu, Y. Hou, S. Gao and S. Sun, *Adv. Mater.*, 2010, **22**, 2729–2742.
22 J. Park, N. R. Kadasala, S. A. Abouelmagd, M. A. Castanares, D. S. Collins, A. Wei and Y. Yeo, *Biomaterials*, 2016, **101**, 285–295.
23 B. Manoury, E. W. Hewitt, N. Morrice, P. M. Dando, A. J. Barrett and C. Watts, *Nature*, 1998, **396**, 695–699.
24 C. Liu, C. Sun, H. Huang, K. Janda and T. Edgington, *Cancer Res.*, 2003, **63**, 2957–2964.
25 V. Andrade, M. Guerra, C. Jardim, F. Melo, W. Silva, J. M. Ortega, M. Robert, M. H. Nathanson and F. Leite, *J. Hepatol.*, 2011, **55**, 626–635.
26 W. Sun, Y. Lin, L. Chen, R. Ma, J. Cao, J. Yao, K. Chen and J. Wan, *Gene*, 2018, **652**, 16–24.
27 E. Dall and H. Brandstetter, *Biochimie*, 2016, **122**, 126–150.
28 B. J. Park, K. H. Choi and K. C. Nam, *J. Nanosci. Nanotechnol.*, 2015, **15**, 7900–7906.
29 C. Liu, C. Sun and K. Janda, *Cancer Res.*, 2003, **63**, 2957–2964.
30 P. Guo, Z. Zhu, Z. Sun, Z. Wang, X. Zheng and H. Xu, *PLoS One*, 2013, **8**, e73090.
31 M. Poreba, *Biol. Chem.*, 2019, **400**, 1529–1550.
32 S. Shabalala, C. J. F. Muller, J. Louw and R. Johnson, *J. Life Sci.*, 2017, **180**, 160–170.
33 A. M. Meredith and C. R. Dass, *J. Pharm. Pharmacol.*, 2016, **68**, 729–741.
34 K. Kalantari, M. Bin Ahmad, K. Shameli and R. Khandanlou, *Int. J. Nanomed.*, 2013, **8**, 1817–1823.
35 W. Hu, M. Ying, S. Zhang and J. Wang, *J. Biomed. Nanotechnol.*, 2018, **14**, 1359–1374.
36 H. Wang, W. Zhu, J. Liu, Z. Dong and Z. Liu, *ACS Appl. Mater. Interfaces*, 2018, **10**, 14475–14482.
37 S. Laurent, D. Forge, M. Port, A. Roch, C. Robic, L. Vander Elst and R. N. Muller, *Chem. Rev.*, 2008, **108**, 2064–2110.
38 E. K. Schlachter, H. R. Widmer, A. Bregy, T. Lönnfors-Weitzel, I. Vajtai, N. Corazza, V. J. Bernau, T. Weitzel, P. Mordasini, J. Slotboom, G. Herrmann, S. Bogni, H. Hofmann, M. Frenz and M. Reinert, *Int. J. Nanomed.*, 2011, **6**, 1793–1800.
39 Y. N. Zhang, W. Poon, A. J. Tavares, I. D. McGilvray and W. C. W. Chan, *J. Controlled Release*, 2016, **240**, 332–348.
40 D. Kalyane, N. Raval, R. Maheshwari, V. Tambe, K. Kalia and R. K. Tekade, *Mater. Sci. Eng., C*, 2019, **98**, 1252–1276.
41 D. Shao, J. Li, X. Zheng, Y. Pan, Z. Wang, M. Zhang, Q. X. Chen, W. F. Dong and L. Chen, *Biomaterials*, 2016, **100**, 118–133.
42 S. Parveen, A. H. Wani, M. A. Shah, H. S. Devi, M. Y. Bhat and J. A. Koka, *Microb. Pathog.*, 2018, **115**, 287–292.